

# Improved Calibration for Panoramic Annular Lens Systems with Angular Modulation

Ding Wang<sup>1</sup>, Junhua Wang<sup>2</sup>, Yuhan Tian<sup>1</sup>, Min Xu<sup>1</sup>, Lingbao Kong<sup>1</sup>

**Abstract**—This paper addresses the challenges of calibrating Panoramic Annular Lens (PAL) systems, which exhibit unique projection characteristics due to their imaging relationship designed to compress blind zones. Traditional camera calibration methods often fail to accurately capture these properties. To resolve this limitation, we propose a novel projection model that incorporates angular modulation, enabling a more accurate representation of the PAL system’s imaging process. This formulation significantly improves the model’s ability to describe the relationship between object space and image space. We evaluate our approach on both synthetic and real-world datasets tailored for PAL cameras. Experimental results demonstrate that the model achieves sub-pixel accuracy, with reprojection errors typically ranging from 0.1 to 0.3 pixels on  $2048 \times 2048$  images when using five distortion terms. This level of precision surpasses existing calibration models for panoramic cameras, making our method particularly suitable for high-accuracy applications. The datasets used in this study are publicly available at <https://github.com/wwendy233/PALcalib>.

## I. INTRODUCTION

Panoramic imaging enables single-shot capture of  $360^\circ$  horizontal field of view (FoV), making it highly valuable for robot navigation, autonomous driving, and environment perception [1], [2]. Among various designs, the Panoramic Annular Lens (PAL) achieves wide FoV with a compact structure and low distortion through double reflections or refractions (see Fig. 1) [3], [4]. A key feature in advanced PAL systems is the introduction of a geometric parameter  $h$  that modulates the incident angle of light rays (as illustrated by  $l_1$  in Fig. 2), enabling active compression of the central blind zone and optimization of the effective focal length [4]. This design enhances imaging quality and supports high-performance applications such as SLAM and semantic understanding [6], [7].

Despite significant advancements in optical design, calibrating PAL cameras remains a challenging task. Standard approaches, such as fisheye and mirror-based calibration methods [8], [10], are not well-suited for PAL systems due to

their inability to adequately account for blind zone compression. These conventional methods struggle with the complex optical path deviations caused by multiple reflections and refractions within PAL systems. They fail to decouple the angular modulation factor  $h$  from distortion, resulting in inaccurate parameter estimation and degraded calibration performance.

To address this limitation, we propose a novel calibration model specifically designed for PAL systems with blind-zone-compression optics. Our main contributions are:

- We propose an improved projection model that explicitly incorporates angular modulation via  $h$ , capturing the unique imaging characteristics of modern PAL systems.
- We validate the model on both synthetic and real-world datasets tailored for PAL. Experimental results show sub-pixel accuracy, with reprojection errors consistently between 0.1 and 0.3 pixels on  $2048 \times 2048$  images – outperforming existing panoramic calibration methods including KB[8], Mei[10], and Scaramuzza[17].

The rest of this paper is organized as follows: Section II reviews related work in omnidirectional camera calibration. Section III details the proposed projection and distortion model. Calibration procedures are described in Section IV, followed by experimental validation and comparison in Section V. We conclude in Section VI.

## II. RELATED WORK

Omnidirectional cameras are commonly classified into fisheye, multi-camera, and catadioptric systems, each requiring different calibration strategies. Fisheye lenses capture wide FoVs using short focal lengths and follow predictable projection laws (e.g., equidistant), allowing reliable calibration with standard tools [8]. Multi-camera arrays synthesize

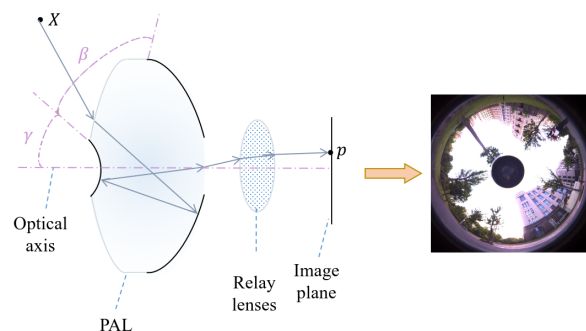


Fig. 1: Schematic diagram of the imaging process for the PAL camera.

<sup>1</sup>Ding Wang is with the School of Information Science and Technology, Fudan University, Shanghai 200433, China [wangd22@m.fudan.edu.cn](mailto:wangd22@m.fudan.edu.cn)

<sup>2</sup>Junhua Wang is with the Institute of Optoelectronics, Fudan University, Shanghai 200438, China [wangjunhua@fudan.edu.cn](mailto:wangjunhua@fudan.edu.cn)

<sup>1</sup>Yuhan Tian is with the School of Information Science and Technology, Fudan University, Shanghai 200433, China [21110720118@m.fudan.edu.cn](mailto:21110720118@m.fudan.edu.cn)

<sup>1</sup>Min Xu is with the School of Information Science and Technology, Fudan University, Shanghai 200433, China [minx@fudan.edu.cn](mailto:minx@fudan.edu.cn)

<sup>1</sup>Lingbao Kong is with the School of Information Science and Technology, Fudan University, Shanghai 200433, China [LKong@fudan.edu.cn](mailto:LKong@fudan.edu.cn)

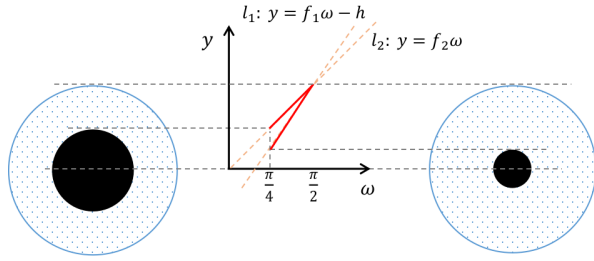


Fig. 2: Two imaging relationships and the effect of  $h$  in compressing the blind zone.  $y$ ,  $\omega$ , and  $f_i$  represent image height, incident ray angle, and focal length, respectively.

panoramic views via image stitching, leveraging equirectangular projection for coordinate mapping [9]; however, they suffer from parallax, exposure mismatch, and increased calibration complexity with scale. Catadioptric systems, such as PALs, use reflective or refractive optics to achieve compact wide-FoV imaging. For instance, Zhou et al. designed a PAL system with a  $360^\circ \times (40^\circ\text{--}95^\circ)$  FoV, which theoretically limits the distortion to 0.5% and achieves experimental distortion below 0.8%, demonstrating its remarkable potential for practical applications [4]. However, their projection relationships and complex optical paths pose challenges for existing calibration methods.

Within this category, parametric models remain widely used. The Kannala-Brandt (KB) model [8] approximates fisheye projection using polynomial radial distortion under the assumption of fixed projection geometry. However, it cannot explicitly model the angular modulation effects in PAL systems, which are instead implicitly absorbed into the distortion coefficients, requiring numerous high-order terms to compensate for geometric variations. The Mei model [10], designed for symmetric mirrors, requires precise knowledge of mirror shape and alignment. Scaramuzza et al.'s method [17] can calibrate generic catadioptric systems without requiring prior knowledge, specifically those with the imaging relationship  $l_2$  in Fig. 2. Nevertheless, these models are ill-suited for PALs with angular modulation and multi-reflection paths.

Unified frameworks aim for broad compatibility. Babel-Calib [13] generates initial parameters via back-projection models and refines them through regression, supporting various central projection cameras. Santana-Cedr s et al. extended iterative two-parameter optimization algorithms for fisheye distortion correction to other omnidirectional systems [16]. Hold-Geoffroy et al.'s perceptual metric for evaluating calibration quality [19], while effective for conventional cameras, remains unvalidated for PAL cameras.

Overall, existing calibration methods perform adequately for traditional panoramic systems, but most neglect the influence of angular modulation in blind zone compression and focal length optimization for PAL cameras. To bridge this gap, this paper introduces an improved calibration model that explicitly incorporates angular modulation parameter, achieving higher accuracy and computational efficiency.

### III. PAL CAMERA MODEL

The PAL camera achieves ultra-wide FoV imaging within a single-camera architecture through a unique optical design [4]. It introduces a parameter  $h$  to optimize blind zone compression and effective focal length optimization (Fig. 2). The core imaging relationship of the PAL system is defined as:

$$y = f \cdot \omega - h = f \cdot (\omega - h'), \quad (1)$$

where  $h' = h/f$  is a constant parameter. By adjusting  $h$ , the model significantly reduces the central blind zone caused by light occlusion in conventional catadioptric systems.

#### A. Radial Symmetric Distortion Model

Radial symmetric distortion, the dominant form of distortion in most optical systems, is characterized by nonlinear radial displacement of light rays. Unlike traditional systems [8], [10], the PAL system requires a revised radial distortion model to account for its unique projection characteristics. The normalized image height containing radial distortion is formulated as:

$$r(\omega) = (\omega - h') + \sum_{i=2}^k a_i (\omega - h')^{2i-1}, \quad (2)$$

where  $a_i$  are radial distortion coefficients. This polynomial model provides sufficient degrees of freedom to approximate the actual projection curves of PAL systems. The impact of the number of distortion terms on the calibration is explored through experiments (Sec. V-A).

#### B. Asymmetric Distortion and Full Imaging Model

Asymmetric distortions, typically caused by lens misalignment or manufacturing imperfections, can be decomposed into radial and tangential components [8]. By introducing an adjusted angular parameter, we define the radial component as:

$$\Delta_r(\omega, \varphi) = [l_1(\omega - h') + l_2(\omega - h')^3 + l_3(\omega - h')^5] \cdot (i_1 \cos \varphi + i_2 \sin \varphi + i_3 \cos 2\varphi + i_4 \sin 2\varphi), \quad (3)$$

and the tangential component as:

$$\Delta_t(\omega, \varphi) = [q_1(\omega - h') + q_2(\omega - h')^3 + q_3(\omega - h')^5] \cdot (j_1 \cos \varphi + j_2 \sin \varphi + j_3 \cos 2\varphi + j_4 \sin 2\varphi), \quad (4)$$

where  $\varphi$  is the azimuthal angle relative to a reference direction;  $l_c, q_c, (c = 1, 2, 3)$  are distortion coefficients for radial and tangential directions;  $i_b, j_b, (b = 1, \dots, 4)$  are modulation coefficients tied to  $\varphi$ . The distorted coordinates  $\mathbf{r}_d(x_d, y_d)$  in the normalized image plane are given by:

$$\mathbf{r}_d = r(\omega) \mathbf{u}_r(\varphi) + \Delta_r(\omega, \varphi) \mathbf{u}_r(\varphi) + \Delta_t(\omega, \varphi) \mathbf{u}_\varphi(\varphi), \quad (5)$$

where  $\mathbf{u}_r(\varphi)$  and  $\mathbf{u}_\varphi(\varphi)$  are unit vectors in the radial and tangential directions, respectively. The final distorted pixel coordinates  $\mathbf{p}(p_x, p_y)$  are obtained via:

$$p_x = m_u x_d + p_{x_0}, \quad p_y = m_v y_d + p_{y_0}, \quad (6)$$

with  $(p_{x_0}, p_{y_0})$  as the principal point and  $m_u, m_v$  as pixel scaling factors in horizontal and vertical directions.

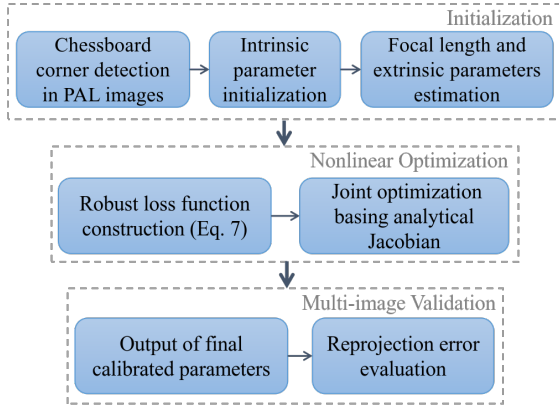


Fig. 3: Overview of the proposed PAL camera calibration pipeline.

#### IV. CALIBRATION STEPS

The proposed calibration method for PAL cameras includes initialization, nonlinear optimization, and multi-image validation processes (see Fig. 3), effectively addressing the limitations of traditional methods in handling distortion coupling and blind zone compression.

##### A. Initialization

The initial parameters are derived from geometric constraints using a planar chessboard pattern. First, we adopt the method proposed in [11] to automatically detect chessboard corners, which is robust to severe distortion and blurred images. The principal point  $(p_{x_0}, p_{y_0})$  is initialized at the image plane centroid  $(W/2, H/2)$ , where  $W$  and  $H$  denote the image width and height, respectively, providing a robust initial estimate for the optical center. Additionally, the parameter  $h'$  is initialized to 0.1, and radial distortion coefficients  $a_i$  are set to zero to establish a baseline undistorted projection model. In our tests, asymmetric distortions contribute minimally to the overall error in PAL cameras. To prioritize computational efficiency and avoid overfitting, this work considers solely radial symmetric distortion during calibration.

For focal length estimation, we perform least-squares circle fitting to each row of detected chessboard corners and compute vanishing points through pairwise circle intersections [20]. To generate focal length candidates, we use the relation  $f_k = |\mathbf{v}_i - \mathbf{v}_j|/\pi$ , where  $\mathbf{v}_i$  and  $\mathbf{v}_j$  represent pairs of vanishing points. For each candidate focal length, the corresponding extrinsic parameters  $R_l, t_l$  for every chessboard pose are estimated using perspective-n-point (PnP) algorithms. The candidate yielding the minimal reprojection error is then selected and utilized to initialize the pixel scaling factors  $m_u$  and  $m_v$ . This initialization strategy provides physically plausible starting values while ensuring numerical stability for subsequent nonlinear optimization.

##### B. Nonlinear Optimization and Validation

Following initialization, a nonlinear least-squares optimization is performed to refine all parameters by minimizing

the following objective function based on reprojection errors:

$$\mathbf{E} = \sum_j \rho \left( \|\mathbf{p}_j - \hat{\mathbf{p}}_j(\mathbf{t})\|^2 \right), \quad (7)$$

where  $\rho(\cdot)$  denotes the Cauchy loss function, which helps suppress the influence of outliers in feature detection. The parameter vector is defined as

$$\mathbf{t} = [h', m_u, m_v, p_{x_0}, p_{y_0}, a_2 \dots a_k, R_0, t_0 \dots R_l, t_l], \quad (8)$$

with  $a_k$  representing the highest-order distortion coefficient and  $l$  indicating the number of chessboard poses. The optimization is implemented using the Ceres Solver with the Levenberg-Marquardt algorithm [21], where intrinsic and extrinsic parameters are jointly optimized. The process terminates when either the parameter update step size or the change in the objective function falls below a convergence threshold, or when the maximum number of iterations is reached. A quaternion-based local parameterization is employed to improve numerical stability and avoid singularities during rotation updates.

For robustness and calibration accuracy, multiple calibration images covering the full FoV are used for global optimization. In the validation phase, the system computes reprojection errors frame-by-frame based on the optimized parameters, and quantitatively evaluates the discrepancies between extracted and reprojected chessboard corners. Experimental results demonstrate that the proposed method achieves sub-pixel reprojection accuracy with minimal computational overhead.

#### V. EXPERIMENTS

To evaluate the performance of the proposed calibration method, experiments are conducted on both real-world and synthetic datasets. Real-world data are captured using PAL cameras with  $360^\circ \times (40^\circ - 95^\circ)$  FoV and  $2048 \times 2048$  resolution, yielding six datasets (S1–S6) under varying environmental conditions. Synthetic data is generated using Blender software [18], simulating a PAL system with identical FoV specifications. Equirectangular images are converted to annular format via the imaging relationship described in Eq. (2), with resolutions of  $2048 \times 2048$  and  $1024 \times 1024$ . Gaussian noise with a standard deviation  $(\sigma)$  ranging from 0 to 10 pixels is added to all synthetic images to analyze the impact of noise and resolution on calibration results.

##### A. Impact of Radial Distortion Term Count

We systematically analyze the trade-off between radial distortion term count  $(n)$  and calibration performance across datasets S1–S6. Figure 5 illustrates the trends in reprojection error and calibration time as  $n$  increases from 2 to 10, where each increment in  $n$  introduces higher-order distortion coefficients (e.g.,  $n = 2$  corresponds to the 3rd- and 5th-order terms with coefficients  $a_2$  and  $a_3$ , respectively).

Results show that increasing  $n$  significantly reduces reprojection error when  $n \leq 5$ , as higher-order terms better capture the nonlinear distortions, especially near the image

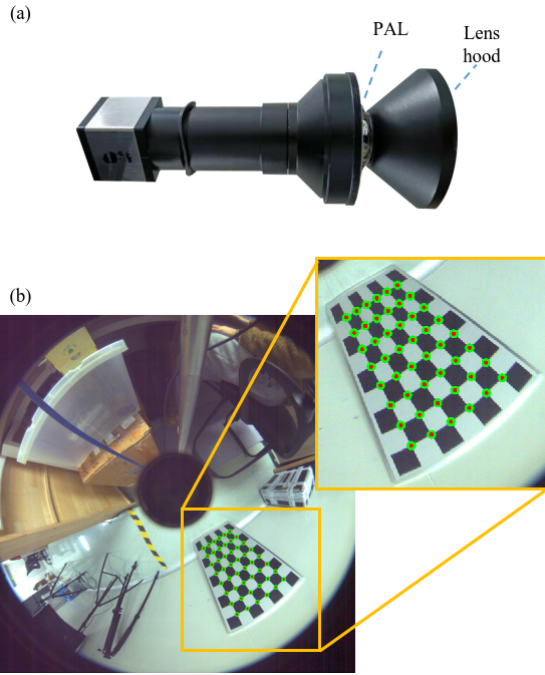


Fig. 4: (a) Physical image of the PAL camera. (b) A chessboard image with the chessboard corners extracted using our method (red dots) and the reprojected results (green circles).

boundary. For instance, on dataset S1, the error is  $0.23 \pm 0.22$  pixels at  $n = 5$ . However, further increasing  $n$  (e.g., to 10) leads to only marginal improvements and occasional fluctuations. Calibration time increases with  $n$ : for S1, it rises from  $30.8s$  at  $n = 5$  to  $83.5s$  at  $n = 10$ . Similar trends are observed in smaller datasets (S2, S3; see Table I), where calibration time remains around  $10s$  for  $n \leq 5$ , but increases significantly for  $n > 5$ . Meanwhile, the reprojection error stabilizes around  $0.15 \pm 0.10$  pixels. As shown in Figure 4b, the reprojected chessboard corners align closely with the detected ones based on our calibration results obtained with  $n = 5$ .

The reprojection error distributions in Fig. 6 show no significant directional bias across views, indicating consistent calibration performance. Each cross ( $\times$ ) represents the end-point of a reprojection error vector, with colors distinguishing errors from different calibration images. The slightly higher errors in datasets S1 and S6 may be attributed to the specific characteristics of the camera and lighting conditions (see example images in the insets). These datasets contain more calibration images, and a few samples with large errors likely result from extreme chessboard poses or low surface brightness, which can affect corner detection accuracy.

Undistortion of PAL images is also performed based on the calibration parameters obtained with  $n = 5$  (Fig. 7). The resulting equirectangular images realistically represent the surrounding  $360^\circ$  scene, including vehicles, trees, and other objects, with minimal geometric distortion. This demonstrates that the method’s robustness and its suitability for real-world applications such as omnidirectional vision and

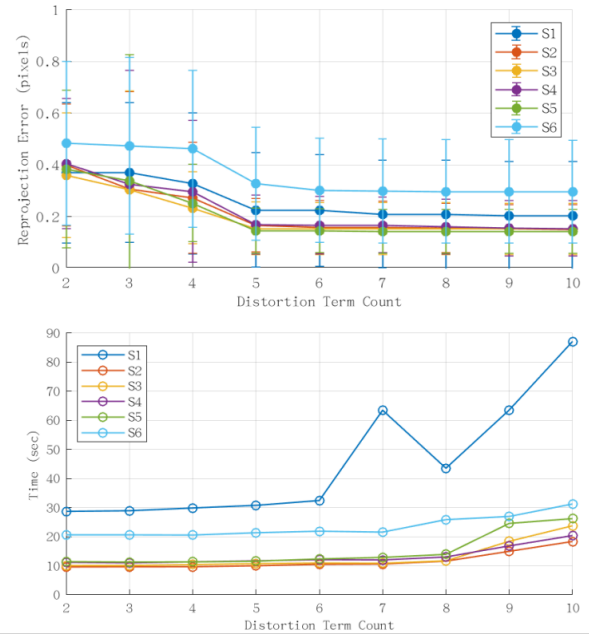


Fig. 5: Calibration results for real-world datasets in different distortion term counts of our method.

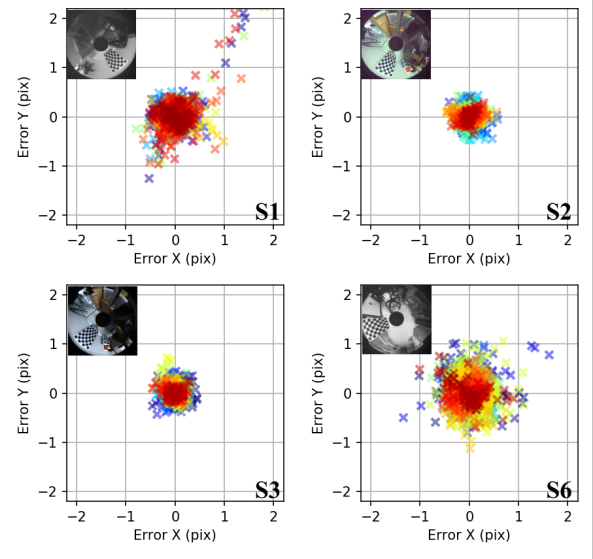


Fig. 6: Reprojection error distribution for real-world dataset calibration with  $n = 5$ . Example images from each dataset are shown as insets.

3D perception, where geometric accuracy is critical.

### B. Accuracy Comparison with Existing Methods

In the analysis of experimental results (see Table I), we compare the reprojection errors of different calibration methods across datasets S1–S6. In our proposed model, N4 and N5 denote the cases where the number of radial distortion terms  $n$  is set to 4 and 5, respectively. N5-AD refers to the full model that further incorporates asymmetric distortion modeling based on N5 (see Sec. III-B). Traditional methods, such as Scaramuzza and Mei, exhibit relatively high





Fig. 7: The effect of distortion correction and unwrapping of the annular image based on our model.

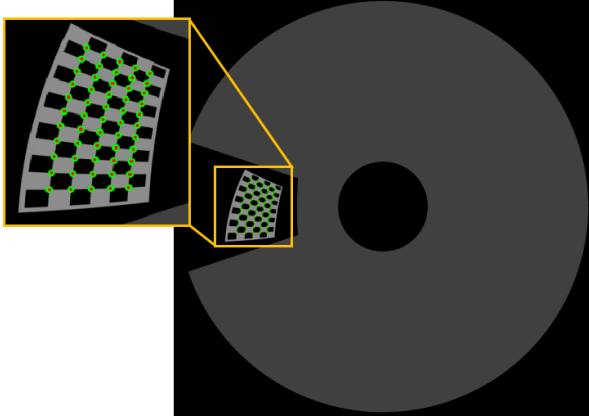


Fig. 8: Chessboard corners extracted from the synthetic image (red dots) and the reprojected results after calibration (green circles).

reprojection errors, ranging from 0.632 to 1.133 pixels and 1.352 to 2.749 pixels, respectively. These results indicate that the Mei method is less suitable for PAL cameras. The KB model performs better, achieving an error range of 0.495 to 0.688 pixels. This suggests that it provides a better fit to the imaging characteristics of PAL cameras compared to previous methods, typically using four distortion terms.

The proposed method further incorporates the effect of angular modulation on the projection relationship, leading to a significant reduction in calibration errors. For N4, reprojection errors range from 0.233 to 0.472 pixels. With N5, which introduces an additional distortion term, the accuracy is further improved. N5-AD achieves the highest accuracy, with the minimum and maximum errors reduced to 0.119 and 0.278 pixels, respectively. In principle, the calibration accuracy of the KB model could be improved by

introducing a few additional higher-order distortion terms, which primarily correct deviations at large radial distances. However, excessive terms increase computational complexity, lead to parameter coupling, and reduce interpretability – an unjustified trade-off given that PAL systems inherently exhibit low distortion. Notably, the parameter  $h$  in Eq. 1 directly influences the central image region and controls the effective radial offset near the optical axis. By explicitly capturing this geometric effect, our model achieves a better fit to PAL-specific imaging characteristics without significantly increasing higher-order distortion terms, avoiding parameter redundancy and runtime inefficiency. As shown in Fig. 5, even with only two distortion terms, the mean reprojection errors of our method remain below 0.5 pixels across all datasets, surpassing the performance of existing methods listed in Table I.

The proposed model also demonstrates strong adaptability across datasets with varying characteristics. For instance, on the complex S6 dataset, the mean reprojection errors of both the Mei and Scaramuzza methods increase significantly, whereas the N5 and N5-AD models achieve mean errors of 0.340 and 0.278 pixels, respectively. On other datasets, the mean reprojection error of N5-AD is consistently reduced by approximately 0.03 pixels compared to N5, indicating that the asymmetric distortion is more pronounced in the S6 dataset. It should be noted that although N5-AD introduces more parameters and achieves higher accuracy, it may pose a risk of overfitting and require longer optimization time when control points do not fully cover the image. Therefore, we suggest setting the number of distortion terms according to the specific application requirements to achieve the desired balance between calibration accuracy and computational efficiency.

### C. Robustness to Noise and Resolution

To further validate the performance of the proposed model, experiments are conducted using a synthetic dataset. The images in these datasets are generated by directly transforming them into annular images based on the imaging relationship (Eq. (2)). Since these images theoretically exhibit minimal distortion, they allow for a clearer evaluation of the calibration method under ideal conditions. Fig. 9 shows the calibration results for the N5 model.

When the noise level is low ( $\sigma \leq 7$  pixels), the calibration error remains at a low level. For instance, at a resolution of  $1024 \times 1024$ , the reprojection error is  $0.07 \pm 0.05$  pixels when  $\sigma = 5$ , and the reprojected corner coordinates are nearly

TABLE I: Mean Reprojection Errors of Different Calibration Models on Real-World Datasets (in pixels).

Dataset	S1	S2	S3	S4	S5	S6
Image Number	40	22	22	23	23	31
Scaramuzza* [17]	0.855	0.632	0.689	0.653	0.781	1.133
Mei* [8]	1.621	1.507	1.352	1.770	1.642	2.749
KB* [10]	0.542	0.495	0.591	0.538	0.622	0.688
N4 (ours)	0.327	0.271	0.233	0.296	0.252	0.472
N5 (ours)	0.225	0.166	0.153	0.168	0.145	0.340
N5-AD (ours)	<b>0.194</b>	<b>0.138</b>	<b>0.126</b>	<b>0.133</b>	<b>0.119</b>	<b>0.278</b>

\* Baselines evaluated using public implementations on our datasets.

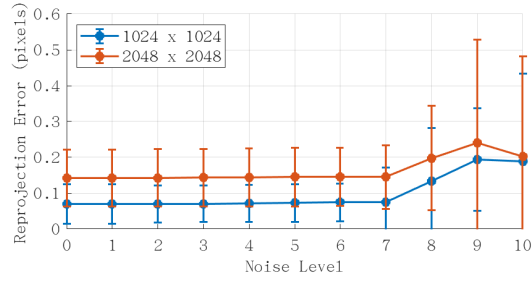


Fig. 9: Calibration results for synthetic datasets with varying noise and resolution.

identical to the extracted ones (see Fig. 8). At the higher resolution of  $2048 \times 2048$ , the error increases slightly to  $0.14 \pm 0.08$  pixels under the same noise level. This indicates that increasing the image resolution results in a marginal increase in error, which remains within an acceptable range. However, when the noise level becomes high ( $\sigma > 7$  pixels), both the mean reprojection error and the standard deviation increase significantly. The slight decrease observed at  $\sigma = 10$  pixels is due to a number of images failing corner detection and being excluded from the optimization. In summary, the proposed method demonstrates strong adaptability and robustness across different resolutions and noise conditions.

## VI. CONCLUSIONS

In this paper, we present a novel calibration method specifically designed for PAL cameras, which exhibit unique projection characteristics due to their imaging relationship designed to compress blind zones. The model incorporates angular modulation, enabling better representation of the PAL system's imaging process. This formulation significantly improves the model's ability to describe the relationship between object space and image space. We validate the proposed model using both synthetic and real-world datasets tailored for PAL cameras. Experimental results demonstrate that the model achieves sub-pixel accuracy, with reprojection errors typically ranging from 0.1 to 0.3 pixels on  $2048 \times 2048$  images when using five distortion terms. This level of precision surpasses existing calibration models for panoramic cameras, making our method particularly suitable for high-accuracy applications such as precision measurement, visual localization and 3D reconstruction.

## ACKNOWLEDGMENT

This work is supported by the National Natural Science Foundation of China (52075100).

## REFERENCES

- [1] S. Gao, K. Yang, H. Shi, K. Wang, and J. Bai, "Review on Panoramic Imaging and Its Applications in Scene Understanding," *IEEE Transactions on Instrumentation and Measurement*, vol. 71, pp. 1-34, 2022.
- [2] Z. Wang, K. Yang, H. Shi, P. Li, F. Gao, J. Bai, and K. Wang, "LF-VISLAM: A SLAM Framework for Large Field-of-View Cameras With Negative Imaging Plane on Mobile Agents," *IEEE Trans. Autom. Sci. Eng.*, vol. 21, no. 4, pp. 6321-6335, 2024.
- [3] D. Wang, J. Wang, Y. Tian, K. Hu, and M. Xu, "PAL-SLAM: a feature-based SLAM system for a panoramic annular lens," *Opt Express*, vol. 30, no. 2, pp. 1099-1113, 2022.

- [4] Q. Zhou, Y. Tian, J. Wang, and M. Xu, "Design and implementation of a high-performance panoramic annular lens," *Applied Optics*, vol. 59, no. 36, pp. 11246-11252, 2020.
- [5] J. Wang, Y. Liang, and M. Xu, "Design of panoramic lens based on ogive and aspheric surface," *Opt Express*, vol. 23, no. 15, pp. 19489-19499, 2015.
- [6] D. Wang, J. Wang, Y. Tian, Y. Fang, Z. Yuan, and M. Xu, "PAL-SLAM2: Visual and visual-inertial monocular SLAM for panoramic annular lens," *ISPRS Journal of Photogrammetry and Remote Sensing*, vol. 211, pp. 35-48, 2024.
- [7] Z. Yuan, J. Wang, Y. Lv, D. Wang, and Y. Fang, "Laformer: Vision Transformer for Panoramic Image Semantic Segmentation," *IEEE Signal Processing Letters*, vol. 30, pp. 1792-1796, 2023.
- [8] J. Kannala and S. S. Brandt, "A Generic Camera Model and Calibration Method for Conventional, Wide-Angle, and Fish-Eye Lenses," *IEEE transactions on pattern analysis and machine intelligence*, vol. 28, no. 8, pp. 1335-1340, 2006.
- [9] A. Torii, M. Havlena and T. Pajdla, "From Google Street View to 3D city models," 2009 IEEE 12th International Conference on Computer Vision Workshops, ICCV Workshops, Kyoto, Japan, 2009, pp. 2188-2195.
- [10] C. Mei and P. Rives, "Single View Point Omnidirectional Camera Calibration from Planar Grids," in *Proceedings 2007 IEEE International Conference on Robotics and Automation*, Roma, 2007, pp. 3945-3950.
- [11] D. Wang, B. Liu, Z. Liu, J. Wang, M. Xu and L. Kong, "LONS-Calib: Extrinsic Calibration of LiDAR and Omnidirectional Camera With Negative Space," in *IEEE Transactions on Instrumentation and Measurement*, vol. 74, pp. 1-13, 2025.
- [12] N. Wakai and T. Yamashita, "Deep Single Fisheye Image Camera Calibration for Over 180-degree Projection of Field of View," presented at the 2021 IEEE/CVF International Conference on Computer Vision Workshops (ICCVW), 2021.
- [13] Y. Lochman, K. Liepiesshov, J. Chen, M. Perdoch, C. Zach, and J. Pritts, "Babelcalib: A universal approach to calibrating central cameras," in *Proceedings of the IEEE/CVF International Conference on Computer Vision*, 2021, pp. 15253-15262.
- [14] F. Camposeco, T. Sattler, and M. Pollefeys, "Non-parametric structure-based calibration of radially symmetric cameras," in *Proceedings of the IEEE International Conference on Computer Vision*, 2015, pp. 2192-2200.
- [15] X. Yin, X. Wang, J. Yu, M. Zhang, P. Fua, and D. Tao, "Fisheyerecnet: A multi-context collaborative deep network for fisheye image rectification," in *Proceedings of the European conference on computer vision (ECCV)*, 2018, pp. 469-484.
- [16] D. Santana-Cedr s, L. G mez, M. Alem n-Flores, A. Salgado, J. Escl rin, L. Mazorra, and L. Alvarez, "An Iterative Optimization Algorithm for Lens Distortion Correction Using Two-Parameter Models," *Image Process. On Line*, vol. 6, pp. 326-364, 2016.
- [17] D. Scaramuzza, A. Martinelli, and R. Siegwart, "A Toolbox for Easily Calibrating Omnidirectional Cameras," in *Proc. IEEE/RSJ Int. Conf. Intell. Robots Syst. (IROS)*, Beijing, China, 2006, pp. 5695-5701.
- [18] Blender Online Community, "Blender - a 3D Modelling and Rendering Package," Blender Foundation, Blender Institute, Amsterdam, 2021. [Online]. Available: <https://www.blender.org>.
- [19] Y. Hold-Geoffroy, K. Sunkavalli, J. Eisenmann, M. Fisher, E. Gambaletto, S. Hadap, and J.-F. Lalonde, "A Perceptual Measure for Deep Single Image Camera Calibration," in *Proc. IEEE Conf. Comput. Vis. Pattern Recognit.*, 2018, pp. 2354-2363.
- [20] C. Hughes, P. Denny, M. Glavin, and E. Jones, "Equidistant Fish-Eye Calibration and Rectification by Vanishing Point Extraction," *IEEE Transactions on Pattern Analysis and Machine Intelligence*, vol. 32, no. 12, pp. 2289-2296, 2010.
- [21] S. Agarwal, K. Mierle, and The Ceres Solver Team, "Ceres Solver," 2023. [Online]. Available: <https://github.com/ceres-solver/ceres-solver>.